

# Multiscale phonon thermal transport in nano-porous silicon

Cite as: Appl. Phys. Lett. **124**, 252202 (2024); doi: [10.1063/5.0205455](https://doi.org/10.1063/5.0205455)

Submitted: 26 February 2024 · Accepted: 9 June 2024 ·

Published Online: 18 June 2024



View Online



Export Citation



CrossMark

B. Kurbanova,<sup>1,a)</sup> D. Chakraborty,<sup>2</sup> A. Abdullaev,<sup>1</sup> A. Shamatova,<sup>1</sup> O. Makukha,<sup>3</sup> A. Belarouci,<sup>3</sup> V. Lysenko,<sup>4</sup> A. Azarov,<sup>5</sup> A. Kuznetsov,<sup>5</sup> Y. Wang,<sup>6</sup> and Z. Utegulov<sup>1,a)</sup>

## AFFILIATIONS

<sup>1</sup>Department of Physics, School of Sciences and Humanities, Nazarbayev University, 010000 Astana, Kazakhstan

<sup>2</sup>School of Physics, University of Bristol, Bristol BS8 1QU, United Kingdom

<sup>3</sup>Lyon Institute of Nanotechnology, UMR 5270, INSA de Lyon, 69100 Villeurbanne, France

<sup>4</sup>Light Matter Institute, UMR-5306, Claude Bernard University of Lyon/CNRS, Université de Lyon, 69622 Villeurbanne Cedex, France

<sup>5</sup>Department of Physics, Center of Materials Science and Nanotechnology, University of Oslo, N-0316 Oslo, Norway

<sup>6</sup>Department of Chemical and Material Engineering, School of Engineering and Digital Sciences, Nazarbayev University, 010000 Astana, Kazakhstan

**Note:** This paper is part of the APL Special Collection on Advances in Thermal Phonon Engineering and Thermal Management.

<sup>a)</sup>Authors to whom correspondence should be addressed: [bayan.kurbanova@nu.edu.kz](mailto:bayan.kurbanova@nu.edu.kz) and [zhutegulov@nu.edu.kz](mailto:zhutegulov@nu.edu.kz)

## ABSTRACT

We performed a comprehensive *multi-scale* phonon-mediated thermal transport study of nano-porous silicon (np-Si) films with average porosities in the range of  $\phi = 30\%$ – $70\%$ . This depth-resolved thermal characterization involves a combination of optical methods, including femtosecond laser-based time-domain thermo-reflectance (TDTR) with MHz modulation rates, opto-thermal micro-Raman spectroscopy, and continuum laser wave-based frequency domain thermo-reflectance (FDTR) with kHz modulation rates probing depths of studied samples over 0.5–1.2, 2–3.2, and 23–34  $\mu\text{m}$ , respectively. We revealed a systematic decrease in thermal conductivity ( $k$ ) with the rise of  $\phi$ , i.e., with the lowering of the Si crystalline phase volumetric fraction. These data were used to validate our semi-classical phonon Monte Carlo and finite element mesh simulations of heat conduction, taking into account disordered geometry configurations with various  $\phi$  and pore size, as well as laser-induced temperature distributions, respectively. At high  $\phi$ , the decrease in  $k$  is additionally influenced by the disordering of the crystal structure, as evidenced by the near-surface sensitive TDTR and Rutherford backscattering spectroscopy measurements. Importantly, the  $k$  values measured by FDTR over larger depths inside np-Si were found to be anisotropic and lower than those detected by the near-surface sensitive TDTR and Raman thermal probes. This finding is supported by the cross-sectional scanning electron microscopy image indicating enhanced  $\phi$  distribution over these micrometer-scale probed depths. Our study opens an avenue for nano-to-micrometer scale thermal depth profiling of porous semiconducting media with inhomogeneous porosity distributions applicable for efficient thermoelectric and thermal management.

Published under an exclusive license by AIP Publishing. <https://doi.org/10.1063/5.0205455>

Effective thermal management at nano- and micro-scales has become critical for various applications involving nano- and micro-electronics and advanced energy transport and conversion. The emergence of 3D integration of devices has underscored the significance of developing materials with low thermal conductivity  $k$  that are also compatible with CMOS technology.<sup>1</sup> Understanding heat transfer in nanostructured materials is important for their integration into nanoelectronics and energy conversion devices like thermoelectric generators and coolers.<sup>2,3</sup> Nano-porous silicon (np-Si), fabricated

through the electrochemical etching of single crystalline silicon wafers (c-Si), exhibits  $k$  that is significantly lower, approximately two-to-three orders of magnitude, compared to that of c-Si. This lower  $k$  is a result of phonon scattering across pore surfaces within complex porous architectures and increased phonon-phonon scattering due to its nanoscale architecture.<sup>4</sup> For this reason, np-Si holds significant technological value as a nanostructured medium for thermoelectrics and numerous on-chip applications requiring thermal isolation. A noteworthy illustration can be found in the realm of Si

sensors and Si-based micro-electromechanical devices.<sup>5,6</sup> The remarkably low  $k$  of highly porous Si forms the foundation for various potential applications, including thermoelectric conversion,<sup>7,8</sup> thermal sensors,<sup>9,10</sup> thermally induced broadband sound emission,<sup>11</sup> and mid-infrared applications.<sup>12</sup> Moreover, optimization of its use in optoelectronic applications, given its remarkable photoluminescent characteristics, requires a good knowledge of its thermal properties. Consequently, this topic has become of much interest in the realm of nanoscale heat transport.<sup>13,14</sup> It is acknowledged that thermal depth profiling is very important for characterization of heat conduction in layered and inhomogeneously structured materials where adhesion, near-surface degradation, corrosion, and phase transformation can take place.<sup>15–18</sup> Thus, a more detailed understanding of thermal depth profiling in np-Si can have valuable practical consequences, because the depth porosity variations impact the phonon transport properties, consequently affecting  $k$  value. In its turn, such depth-dependent variation of  $k$  opens broader adjustment possibilities, which can be of interest in thermoelectric and thermal management applications.

The fundamental approach to heat transport measurements consistently involves introducing a heat source that disperses within and around the sample. This process entails tracking the dispersion of heat and then comparing it to a model founded on the principles of thermal diffusion to extract the targeted thermal properties. Various thermal metrologies such as photo-acoustics,<sup>19,20</sup>  $3\omega$ ,<sup>21,22</sup> lock-in thermography,<sup>23</sup> and optical pump-probe method<sup>24</sup> have been employed to study  $k$  as a function of porosity, the morphology and structure<sup>25</sup> of the np-Si samples, the type of initial c-Si substrate,<sup>26</sup> its resistivity,<sup>27</sup> and the electrochemical fabrication.<sup>28</sup> The micro-Raman spectroscopy and scanning thermal microscopy were used to extract the local  $k$  of several types of meso-porous and nanostructured Si

materials.<sup>29–33</sup> Lock-in thermography on np-Si demonstrated thermal anisotropy in cross-plane vs in-plane directions due to the higher inter-connection of the porous structure along the etching direction.<sup>23,34</sup>

However, there have not been prior studies on *multi-scale depth profiling of thermal transport in np-Si*. For that reason, in this work, we performed a comprehensive *multi-scale* phonon-mediated thermal transport study of np-Si films with average porosities in the range of  $\varphi = 30\%–70\%$ . This depth-resolved thermal characterization involves a combination of optical methods including femtosecond laser-based time-domain thermo-reflectance (TDTR) with MHz modulation rates, opto-thermal micro-Raman spectroscopy, and continuum laser wave-based frequency domain thermo-reflectance (FDTR) with kHz modulation rates probing depths of studied porous media over 0.5–1.2, 2–3.2, and 23–34  $\mu\text{m}$ , respectively. In TDTR and FDTR approaches, the heat penetration depth was controlled by modulating the laser pump beams at 1–10 MHz and 1–100 kHz rates, respectively. The micro-Raman spectral thermometry-based heat conduction measurements were used to validate finite element mesh (FEM) simulations of temperature distribution resulting from laser-induced heating in np-Si films. The semi-classical Monte Carlo (MC) simulations of phonon transport were conducted with various disordered geometries to assess the impact of the corresponding porosities and nano-pore size distributions.

In our study, the np-Si films were prepared by subjecting p-type boron-doped (100)-oriented c-Si wafers with a resistivity of  $\sim 10$  to 20  $\text{m}\Omega\cdot\text{cm}$  to electrochemical anodization. The values of  $\varphi = 30\%–70\%$  in the fabricated np-Si film samples are assessed by gravimetric method. The thicknesses of films and pore sizes are measured to be in the range of 23–34  $\mu\text{m}$  and  $D = 13–25$  nm, respectively, as determined by scanning electron microscopy (SEM) (Figs. 1, 4, and 6). The fabrication process as well as the procedure for conducting Raman spectroscopy measurements are provided in the [supplementary material](#).

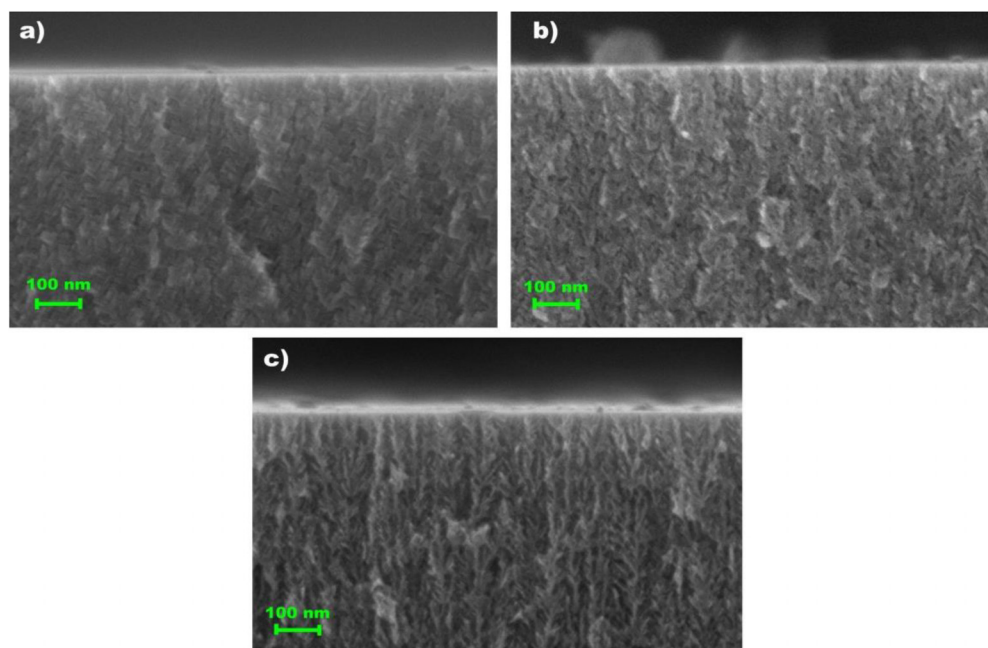


FIG. 1. High-resolution cross-sectional SEM images of np-Si samples depicting the average porosities of  $\varphi =$  (a) 30%, (b) 50%, and (c) 70%.

The primary Raman peak at  $\sim 520\text{ cm}^{-1}$ , associated with the cubic Si LO phonon mode in np-Si, as shown in Fig. 2(a), undergoes a frequency downshift with the rise of 532 nm wavelength incident optical power delivered by laser beam focused on studied samples down to a spot having  $2\text{ }\mu\text{m}$  diameter. The resulting local laser-induced temperature rise was determined from measured Raman Stokes/anti-Stokes integrated peak intensity ratio.<sup>35</sup> Figure 2(b) demonstrates the corresponding changes in temperature  $T$  induced by laser irradiation of np-Si films exhibiting  $\phi$  variations. Films with higher  $\phi$  experience greater heating compared to those with lower  $\phi$ , attributed to the reduced volume fraction of highly conductive c-Si phase in np-Si samples. The measured local temperature values were used to validate our 3D FEM simulations of photo-induced temperature excursions in np-Si performed using the Ansys Lumerical heat module [Fig. 2(c)]. The steady-state Fourier heat conduction equation was solved numerically using absorbed laser light through the np-Si depth ( $2\text{--}3.2\text{ }\mu\text{m}$ ) for the samples with  $\phi = 30\%\text{--}70\%$ . The optical absorption depth values were extracted by assessing the absorption coefficient values obtained from both literature and our own ellipsometry data (refer to the [supplementary material](#) for detailed explanations of the ellipsometry measurement process and assessment of the absorption depth values). The ellipsometry measurements required the knowledge of the real and imaginary parts of the refractive index, which were found using

Bruggeman effective medium approximation (EMA),<sup>36</sup> which took into account the dielectric constant of air. The resulting temperature distribution, caused by laser heating in np-Si, was assessed with the  $k$  values of the np-Si films used as single-fitting parameters. Since the thicknesses ( $23\text{--}34\text{ }\mu\text{m}$ ) of our samples are much larger than the diameter of the incident laser beam ( $2\text{ }\mu\text{m}$ ) used in Raman thermometry, the incident laser beam was treated as a localized heating source resulting in nearly hemispherical temperature distributions across the np-Si films.

Rutherford backscattering spectroscopy (RBS)/C (channeling) and RBS/R (random) measurements, which probe microstructure down to a depth of  $\sim 1\text{ }\mu\text{m}$ , were employed to assess how changes in crystalline structure and oxidation degree impact *near-surface*  $k$  values. In samples with low porosities ( $\phi = 30\%\text{--}50\%$ ), the crystalline structure remains unaltered. However, at  $\phi \geq 60\%$ , the disorder in the crystalline lattice becomes quite substantial, as seen from the elevated magnitude of the RBS/C spectrum for the samples with  $\phi = 60\%$  and  $70\%$  as seen in Fig. 3.

Subsequently, TDTR measurements, probing depths at  $0.5\text{--}1.2\text{ }\mu\text{m}$  (depending on the porosity level, Table I), reveal a decrease in  $k$  values with the rise of  $\phi$  (excluding that for the  $\phi = 30\%$ ), see Fig. 7 below. The decrease in the near-surface  $k$  in highly porous samples is connected to both the decrease in the c-Si volume fraction and the

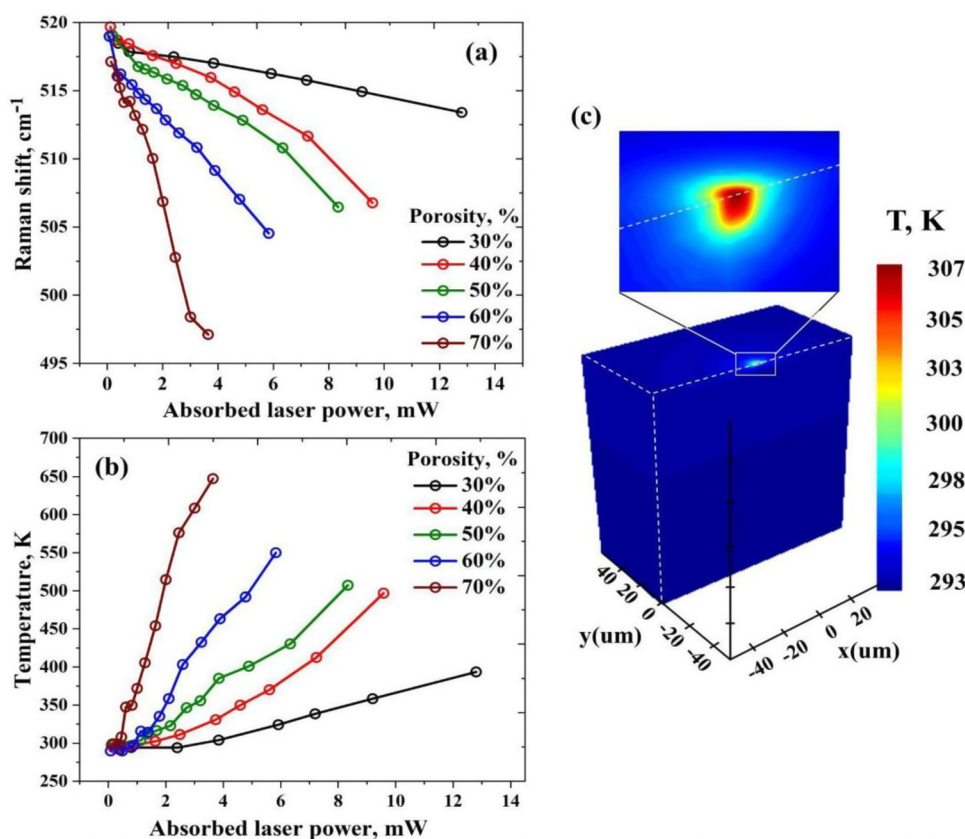


**FIG. 2.** (a) Laser-induced Raman shifts and (b) corresponding measured local temperatures in np-Si layers with various porosities. (c) Typical FEM simulated spatial temperature distribution in np-Si with 30% porosity.

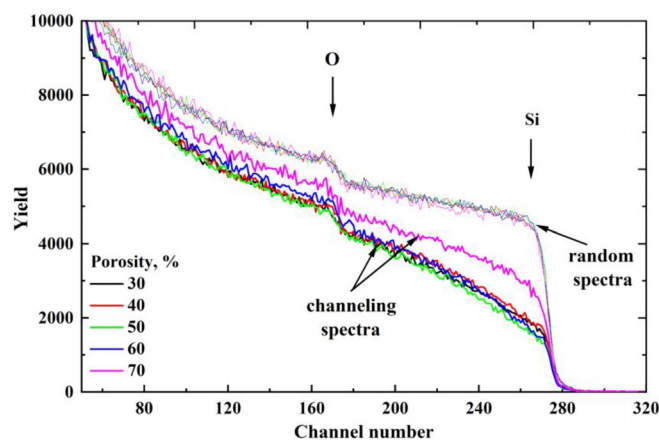


FIG. 3. RBS spectra of np-Si samples having different porosities.

emergence of disorders in the crystalline lattice. However, at low porosities, the reduction in the volumetric fraction determines the change of the  $k$  values. Furthermore, the 70% porous sample exhibits an O/Si ratio of 0.3/0.7, whereas other porosities maintain an equal O/Si ratio of 0.25/0.75, as evident from the derived RBS/R spectra results (Fig. 3) using SIMNRA code.<sup>37</sup> The 70% porous sample will likely be covered by the native oxide layer. However, this top layer has thickness  $<2$  nm, and it is non-continuous on the top surface of np-Si, i.e., does not cover the entire film surface. Therefore, its effect on thermal transport of underlying np-Si samples is negligible,<sup>29</sup> since all our measurement techniques probe heat conduction on a much deeper scale, as seen in Table I. The details of the TDTR, RBS/C, and RBS/R methodologies are described in the supplementary material.

FDTR measurements were conducted to assess the  $k$  values on the depths scale of tens of micrometer inside the np-Si films. Obtained  $k$  values are found to be lower than those probed in the near-surface ( $\sim 1 \mu\text{m}$ ) regions as assessed by TDTR and Raman. The reduced  $k$  is associated with an enhanced distribution of porosity throughout the thickness of the np-Si, as illustrated in Fig. 4, where the dark vertical lines correspond to pore agglomerates. In order to see if thermal anisotropy is present in np-Si samples, we conducted sensitivity analysis presented in Fig. S6(b) of the supplementary material. A good sensitivity to both cross-plane thermal conductivity  $k_z$  and anisotropy ratio  $\eta = k_r/k_z = 1$  (the ratio of in-plane to cross-plane thermal conductivities) is observed. Thus, FDTR data are analyzed using three fitting parameters, i.e.,  $k_z$ ,  $\eta$ , and  $R_0$ . As a result, in Fig. 7, in addition to other thermal transport measurements and Monte Carlo simulations, we

also present our FDTR results by showing both  $k_r$  and  $k_z$  values vs porosity in np-Si samples. Almost all samples demonstrate some thermal anisotropy defined by  $\eta \sim 0.6$ . The difference in anisotropy values compared to the previous works<sup>23,34</sup> is explained by the difference in the etching fabrication process and thermal measurement methods.

In both TDTR and FDTR measurements, for accurate determination of heat conductivity, an EMA model was used [defined by Eq. (S4) of the supplementary material] to take into account the specific heat capacity of air present in the pores of np-Si samples.

Regarding the 30% porous sample, the significant variation in  $k$  values (Fig. 7) can be attributed to the subsurface non-uniform distribution of pore agglomerates both with respect to depth and radial distribution as can be seen from Fig. 4(a). TDTR measurements were conducted over small depths but at larger lateral areas compared to other methods. Consequently, the significant low  $k$  value, measured by TDTR, can be attributed to the probed large pore volume fractions, as numerous pore agglomerates in this 30% porous sample are located near the surface. Thermally probed domain volumes probed by the TDTR, FDTR, Monte Carlo, and Raman-FEM techniques for different porosities can be found from Table I.

A Monte Carlo (MC) method has been adopted for a semi-classical particle-based description of phonon transport in np-Si. The simulation domain is populated with nanostructured features as shown in Fig. 5. We use the “single-phonon” MC approach, which differs from the multi-phonon MC approach described earlier<sup>38–47</sup> and in the supplementary material in terms of phonon attribute book-keeping. The single-phonon method is computationally simpler. By eliminating the need to track multiple phonon positions concurrently, it reduces both the computational complexity and the required resources.<sup>43–46,48,49</sup>

In short, phonons are initialized in the contacts only, based on polarization, frequency, group velocity, and energy. Phonon probabilities are determined by the phonon dispersion relation  $\omega(q)$ , in accordance with the Bose–Einstein statistics at a given temperature.<sup>50</sup> We use  $\omega(q)$  and corresponding group velocities  $v_g(q)$ , as described by Pop *et al.*<sup>41</sup> Phonons then propagate through the simulation domain and alternate between durations of free flight and scattering events. The net sum of the corresponding phonon energies that enter/exit at the hot and cold contact junctions gives the average phonon energy flux (net thermal flow) of np-Si that is then used to determine its thermal conductivity. The detailed explanation of this simulation procedure is systematically described in our previous works.<sup>43–47</sup> The contribution of optical phonons was assumed to be negligible as they have low  $v_g(q)$ .<sup>39,40,42,51,52</sup> The basic porous geometry used in our simulations is illustrated in Fig. 5(b). As given by previous works, all phonons that impinge on a pore boundary scatter, and none are allowed to

TABLE I. Approximate volumes of thermally probed domains (heat penetration depth  $\times$  laser beam area) probed by the TDTR, FDTR, Monte Carlo, and Raman-FEM techniques (computational domain areas) for various samples.

Methods	30%	40%	50%	60%	70%
TDTR	$(1.25 \times 13^2)\pi \mu\text{m}^3$	$(0.94 \times 13^2)\pi \mu\text{m}^3$	$(0.86 \times 13^2)\pi \mu\text{m}^3$	$(0.72 \times 13^2)\pi \mu\text{m}^3$	$(0.49 \times 13^2)\pi \mu\text{m}^3$
FDTR	$(27.8 \times 1^2)\pi \mu\text{m}^3$	$(34 \times 1^2)\pi \mu\text{m}^3$	$(23 \times 1^2)\pi \mu\text{m}^3$	$(30.7 \times 1^2)\pi \mu\text{m}^3$	$(31.5 \times 1^2)\pi \mu\text{m}^3$
Raman-FEM	$(2 \times 2^2)\pi \mu\text{m}^3$	$(2.3 \times 2^2)\pi \mu\text{m}^3$	$(2.4 \times 2^2)\pi \mu\text{m}^3$	$(3 \times 2^2)\pi \mu\text{m}^3$	$(3.2 \times 2^2)\pi \mu\text{m}^3$
Monte-Carlo	$0.5 \times 1 \mu\text{m}^2$	$0.5 \times 1 \mu\text{m}^2$	$0.5 \times 1 \mu\text{m}^2$	$0.5 \times 1 \mu\text{m}^2$	$0.5 \times 1 \mu\text{m}^2$



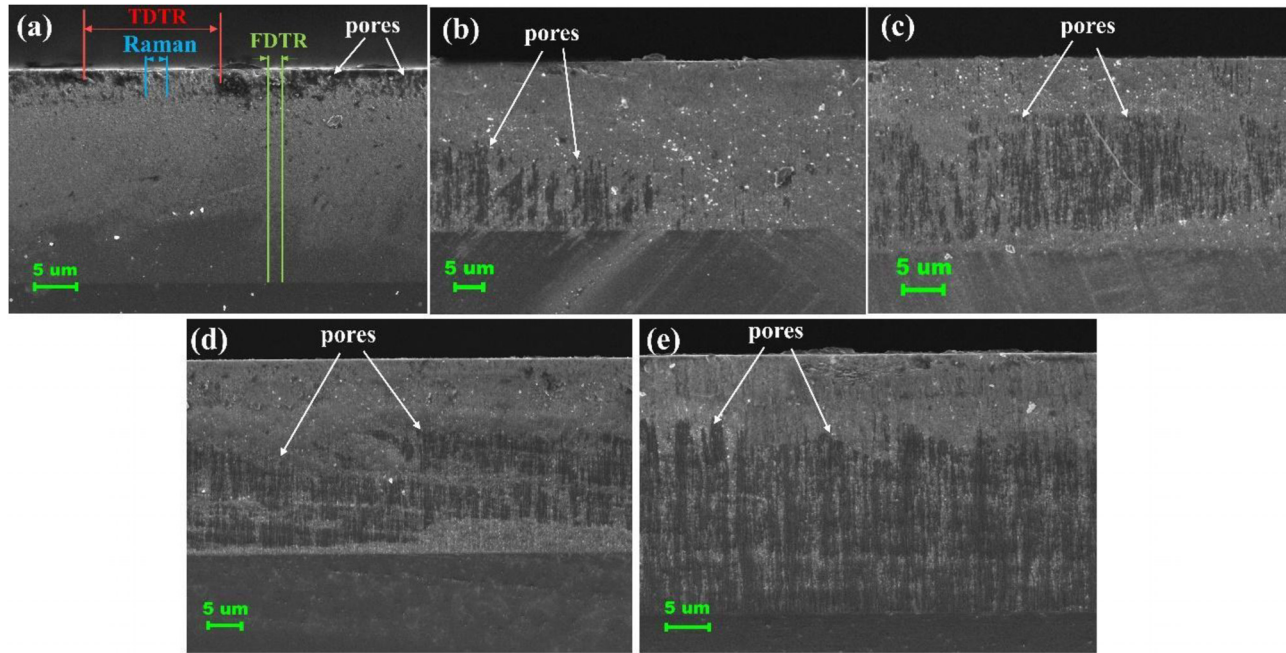


FIG. 4. Low-magnification cross-sectional SEM images of np-Si samples with  $\varphi =$  (a) 30%, (b) 40%, (c) 50%, (d) 60%, and (e) 70%.

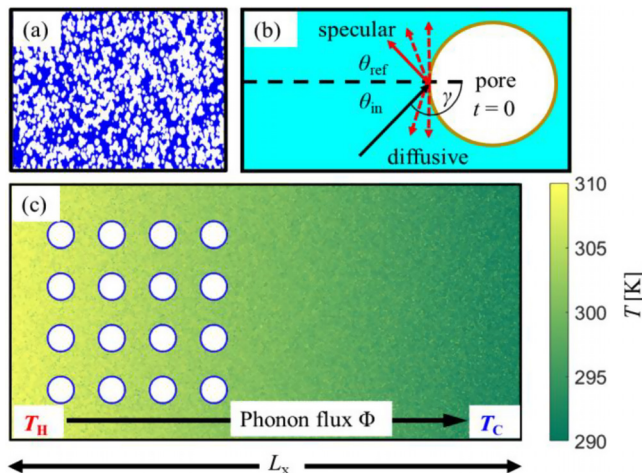
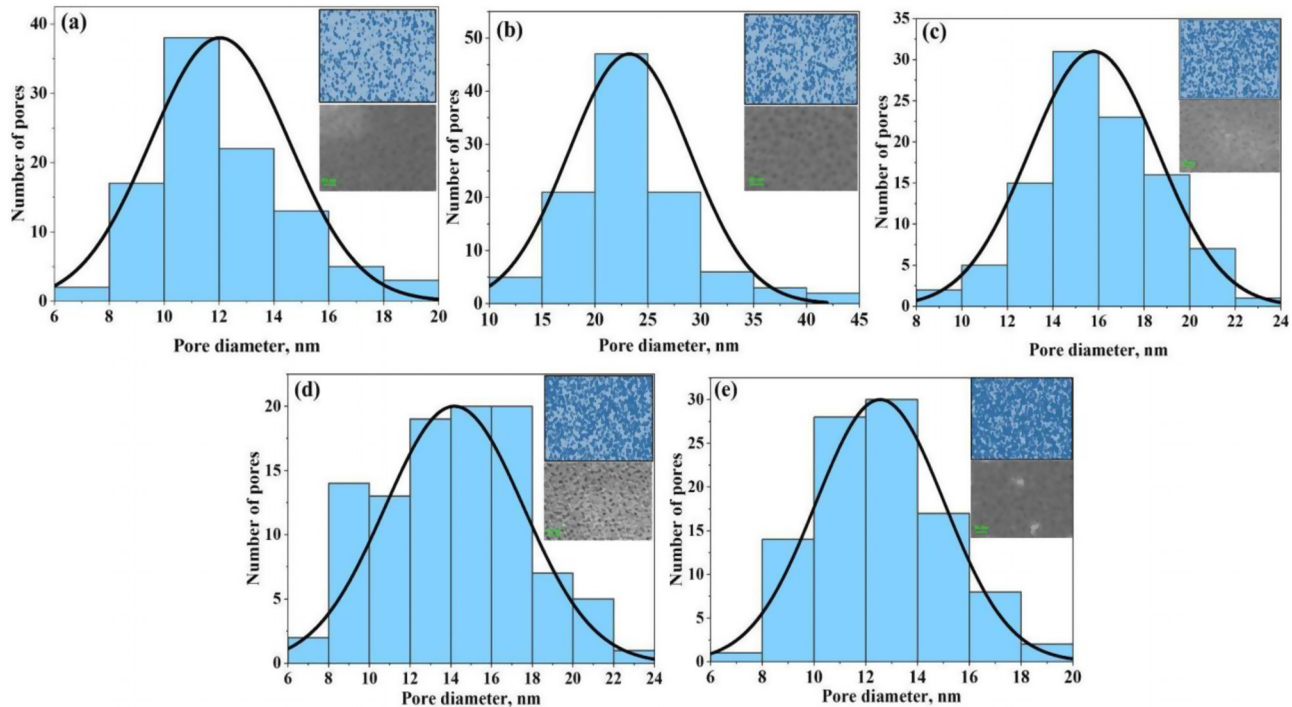


FIG. 5. (a) Example of actual simulated geometry of np-Si with  $\varphi = 60\%$ . White regions depict porous (air) regions with no phonon transmission, while blue regions depict regions of c-Si phase across which phonons can propagate. (b) Schematic of the scattering mechanism for pore scattering, indicating the pore boundary, the initial angle of the phonon  $\theta_{in}$  and potential new angle of propagation  $\theta_{ref}$  depending on specularly parameter  $p$ . Probable paths of the phonon after scattering for both diffusive (red dashed lines) and specular (red solid line) are also depicted. (c) Schematic of the simulation domain with an example of ordered nano-porous geometry. The coloring profile indicates the established thermal gradients when the left and right contacts are set to  $T_H = 310$  K (yellow) and  $T_C = 290$  K (green), respectively.

transmit.<sup>45,48</sup> When a phonon is reflected, then a random number that depends on the roughness of the pore domain, labeled as  $p$ , governs specular or diffuse scattering.<sup>38</sup> As in previous works,<sup>43–46,48,49</sup> we do not assume that the phonon changes its energy at the interface as is common practice, but only its direction. The factor  $p$  ranges from 0 to 1, with  $p=0$  indicating purely diffusive and randomized reflection angle and with  $p=1$  indicating purely specular reflection where the angle of incidence is equal to the angle of reflection [see Fig. 5(b)]. In our case, we use  $p=0.1$  corresponding to a roughness  $\Delta_{rms} \sim 0.3$  nm, which has been shown to correspond well to rough Si surfaces<sup>43</sup> and agrees well with our experimental observations, as outlined in the results section below.

In the case of our porous geometries, the pores are defined as regions of zero transmission within a c-Si matrix, as implemented previously using the same MC methodology for porous Si media with  $\varphi \leq 50\%$ <sup>43,44,48,49</sup> and even with  $\varphi = 70\%$ .<sup>52</sup> More importantly, the uncertainty of  $\pm 0.2$  W/mK in the thermal conductivity of np-Si with  $\varphi = 70\%$  computed by MC method is an order of magnitude larger than the heat conductivity of the air itself (0.03 W/mK),<sup>53</sup> which justifies the use of zero phonon transmission through air pores.

In the simulated schematics [Fig. 5(a)], the porous regions are given in white, while the c-Si phase regions are given in blue. The pores are randomized in both position and size, as encountered in realistic np-Si media. The development of these porous geometries with randomized pores is already well examined in our previous works.<sup>43–45</sup> The position distribution of the pores was taken to be randomly distributed, as in previous works in the literature.<sup>43,44,48</sup> Additionally, in



**FIG. 6.** Top-plane SEM images (insets) with corresponding image processing yielding Gaussian pore size distributions and pore areas of np-Si samples having different  $\phi$  s measured by gravimetry: (a) 30%, (b) 40%, (c) 50%, (d) 60%, and (e) 70%.

this work, we use the top-plane SEM images (Fig. 6) of the np-Si materials to determine the size distribution of pore diameters  $D$ . This was then used to inform the size distribution of the simulated pores.

Near-surface conductivities assessed by Raman and TDTR techniques were found to be in general agreement with conductivity computed by Monte Carlo modeling, as seen in Fig. 7. At the same time, the difference between micrometer-scale depth-sensitive in-plane and cross-plane conductivity values measured by FDTR and those

calculated by MC method is larger. This discrepancy could be explained by structural inhomogeneity of np-Si thin film samples taking place over thermally probed depths down to 23–34  $\mu\text{m}$ , which is not accounted for in Monte Carlo methodology for which computation domain = 0.5–1  $\mu\text{m}$ .

In conclusion, we presented a multi-scale thermal depth profiling characterization across thick np-Si films with  $\phi = 30\%$ –70%. The results from micro-Raman thermometry combined with FEM simulations indicate that the  $k$  of np-Si decreases with increasing  $\phi$ , suggesting a lower volume fraction of c-Si content. Near-surface TDTR measurements, along with RBS results, reveal that the reduction in  $k$  is additionally influenced by the disordering of the crystal structure at high  $\phi$ . Our  $k$  values measured by Raman and TDTR optical techniques are in general agreement with those obtained by semi-classical Monte Carlo phonon transport simulations treating configurations of disordered np-Si architectures with various  $\phi$  and  $D$  distributions. Furthermore, FDTR measurements demonstrate that np-Si becomes more thermally insulative at deeper micrometer-scale depths due to the rise of  $\phi$  as evidenced from cross-sectional SEM imaging, structurally inhomogeneous, and thermally anisotropic in behavior ( $\eta \sim 0.6$ ). We envision applications of these porous semiconductors in advanced thermoelectric and thermal management devices where heat conduction needs be effectively controlled at various nano- and micro-scale depths.

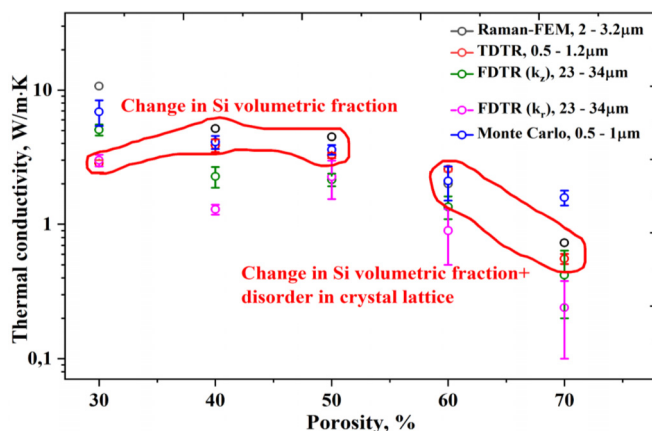


**FIG. 7.** TDTR, FDTR, Raman measurement, and Monte Carlo simulation results for the porosity-dependent thermal conductivity of np-Si.

See the [supplementary material](#) for detailed information about the np-Si fabrication process and structural characterization measurements, Monte Carlo simulation details, and Raman, ellipsometry, and TDTR and FDTR measurement conditions.

The funding by MSHE Nos. AP19679332, NU 20122022CRP1608, NU 11022021CRP1504, and NU 20122022FD4130 grants is acknowledged. The international collaboration was in part enabled by the INTPART Program funded by the Research Council of Norway (Project No. 322382).

## AUTHOR DECLARATIONS

### Conflict of Interest

The authors have no conflicts to disclose.

## Author Contributions

**B. Kurbanova:** Conceptualization (equal); Data curation (equal); Formal analysis (equal); Investigation (equal); Writing – original draft (equal); Writing – review & editing (equal). **D. Chakraborty:** Data curation (equal); Investigation (equal); Software (equal). **A. Abdullaev:** Data curation (equal); Investigation (equal); Methodology (equal). **A. Shamatova:** Conceptualization (equal); Data curation (equal); Investigation (equal); Methodology (equal). **O. Makukha:** Investigation (equal); Software (equal). **A. Belarouci:** Conceptualization (equal); Formal analysis (equal); Investigation (equal); Writing – review & editing (equal). **V. Lysenko:** Investigation (equal); Methodology (equal). **A. Azarov:** Conceptualization (equal); Data curation (equal); Investigation (equal). **A. Kuznetsov:** Funding acquisition (equal); Investigation (equal); Supervision (equal); Writing – review & editing (equal). **Y. Wang:** Conceptualization (equal); Software (equal); Writing – review & editing (equal). **Z. Utegulov:** Conceptualization (equal); Formal analysis (equal); Funding acquisition (equal); Investigation (equal); Methodology (equal); Project administration (equal); Resources (equal); Supervision (equal); Validation (equal); Writing – original draft (equal); Writing – review & editing (equal).

## DATA AVAILABILITY

The data that support the findings of this study are available from the corresponding authors upon reasonable request.

## REFERENCES

- A. M. Massoud, P. O. Chapuis, B. Canut, and J. M. Bluet, *J. Appl. Phys.* **128**, 175109 (2020).
- D. Zhao and G. Tan, *Appl. Therm. Eng.* **66**, 15–24 (2014).
- D. K. Aswal, R. Basu, and A. Singh, *Energy Convers. Manage.* **114**, 50–67 (2016).
- P. Newby, B. Canut, J. M. Bluet, S. Gomès, M. Isaiev, R. Burbelo, K. Termentzidis, P. Chantrenne, L. G. Fréchette, and V. Lysenko, *J. Appl. Phys.* **114**, 014903 (2013).
- M. Capelle, J. Billoue, P. Poveda, and G. Gautier, *Int. J. Microwave Wireless Technol.* **6**, 39–43 (2014).
- G. Kaltsas and A. G. Nassiopoulou, *Sens. Actuators* **76**, 133–138 (1999).
- E. Hourdakis and A. G. Nassiopoulou, *Sensors* **13**, 13596–13608 (2013).
- J. H. Lee, G. A. Galli, and J. C. Grossman, *Nano Lett.* **8**, 3750–3754 (2008).
- E. Hourdakis, P. Sarafis, and A. G. Nassiopoulou, *Sensors* **12**, 14838–14850 (2012).
- D. N. Pagonis, A. Petropoulos, G. Kaltsas, A. G. Nassiopoulou, and A. Tserepi, *Phys. Status Solidi* **204**, 1474–1479 (2007).
- N. Koshida, D. Hippo, M. Mori, H. Yanazawa, H. Shinoda, and T. Shimada, *Appl. Phys. Lett.* **102**, 123504 (2013).
- Z. Wang, J. Zhang, S. Xu, L. Wang, Z. Cao, P. Zhan, and Z. Wang, *J. Phys. D: Appl. Phys.* **40**, 4482–4484 (2007).
- G. Chen, *Nanoscale Energy Transport and Conversion* (Oxford University Press, New York, 2005).
- Z. Zhang, *Nano/Microscale Heat Transfer* (McGraw Hill, New York, 2007).
- T. T. N. Lan, U. Seidel, H. G. Walther, G. Goch, and B. Schmitz, *J. Appl. Phys.* **78**, 4108 (1995).
- A. Sizov, D. Cederkrantz, L. Salmi, A. Rosén, L. Jacobson, S. E. Gustafsson, and M. Gustavsson, *Rev. Sci. Instrum.* **87**, 074901 (2016).
- A. Abdullaev, A. Koshkinbayeva, V. Chauhan, Z. Nurekeyev, J. O’Connell, A. J. Vuuren, V. Skuratov, M. Khafizov, and Z. N. Utegulov, *J. Nucl. Mater.* **561**, 153563 (2022).
- A. Abdullaev, V. S. Chauhan, B. Muminov, J. O’Connell, V. A. Skuratov, M. Khafizov, and Z. N. Utegulov, *J. Appl. Phys.* **127**, 035108 (2020).
- Q. Shen and T. Toyoda, *Rev. Sci. Instrum.* **74**, 601 (2003).
- P. Lishchuk, D. Andrusenko, M. Isaiev, V. Lysenko, and R. Burbelo, *Int. J. Thermophys.* **36**, 2428 (2015).
- A. Melhem, D. D. S. Meneses, C. Andreazza-Vignolles, T. Defforge, G. Gautier, N. Semmar, and C. Andreazza-Vignolle, *J. Phys. Chem. C* **119**, 21443–21451 (2015).
- K. Valalaki and A. G. Nassiopoulou, *J. Phys. D: Appl. Phys.* **50**, 195302 (2017).
- A. Wolf and R. Brendel, *Thin Solid Films* **513**, 385–390 (2006).
- U. Bernini, S. Lettieri, P. M. Maddalena, R. Vitiello, and G. D. Francia, *J. Phys.: Condens. Matter* **13**, 1141–1150 (2001).
- J. D. Boor, D. S. Kim, X. Ao, D. Hagen, A. Cojocar, H. Foll, and V. Schmidt, *EPL* **96**, 16001 (2011).
- S. Lettieri, U. Bernini, E. Massera, and P. M. Maddalena, *Phys. Status Solidi C* **2**, 3414–3418 (2005).
- K. Dubyk, A. Pastushenko, T. Nychporuk, R. Burbelo, M. Isaiev, and V. Lysenko, *J. Phys. Chem. Solids* **126**, 267 (2019).
- G. Benedetto, L. Boarino, and R. Spagnolo, *Appl. Phys. A* **6**, 155–159 (1997).
- V. Lysenko, S. Périchon, B. Remaki, D. Barbier, and B. Champagnon, *J. Appl. Phys.* **86**, 6841–6846 (1999).
- O. Makukha, I. Lysenko, and A. Belarouci, *Nanomaterials* **13**, 310 (2023).
- B. A. Kurbanova, G. K. Mussabek, V. Y. Timoshenko, V. Lysenko, and Z. N. Utegulov, *Nanomaterials* **11**, 2379 (2021).
- S. Gomes, L. David, V. Lysenko, A. Descamps, T. Nychporuk, and M. Raynaud, *J. Phys. D: Appl. Phys.* **40**, 6677–6683 (2007).
- V. Poborchii, N. Uchida, Y. Miyazaki, T. Tada, P. I. Geshev, Z. N. Utegulov, and A. Volkov, *Int. J. Heat Mass Transfer* **123**, 137–142 (2018).
- K. Kim and T. E. Murphy, *J. Appl. Phys.* **118**, 154304 (2015).
- M. Balkanski, R. F. Wallis, and E. Haro, *Phys. Rev. B* **28**, 1928–1934 (1983).
- B. Fodor, T. Defforge, E. Agócs, M. Fried, G. Gautier, and P. Petrik, *Appl. Surf. Sci.* **421**, 397–404 (2016).
- M. Mayer, *AIP Conf. Proc.* **475**, 541–544 (1999).
- E. Pop, S. Sinha, and K. E. Goodson, *Proc. IEEE* **94**(8), 1587–1601 (2006).
- D. Lacroix, K. Joulain, and D. Lemonnier, *Phys. Rev. B* **72**(6), 064305 (2005).
- S. Mazumdar and A. Majumdar, *ASME J. Heat Transfer* **123**, 749–759 (2001).
- E. Pop, R. W. Dutton, and K. E. Goodson, *J. Appl. Phys.* **96**(9), 4998–5005 (2004).
- Q. Hao, G. Chen, and M. S. Jeng, *J. Appl. Phys.* **106**(11), 114321 (2009).
- D. Chakraborty, S. Foster, and N. Neophytou, *Phys. Rev. B* **98**, 115435 (2018).
- D. Chakraborty, S. Foster, and N. Neophytou, *Mater. Today Proc.* **8**, 652 (2019).
- D. Chakraborty, J. Brooke, N. C. S. Hulse, and N. Neophytou, *J. Appl. Phys.* **126**, 184303 (2019).
- D. Chakraborty, H. Karamitaheri, L. Oliveira, and N. Neophytou, *Comput. Mater. Sci.* **180**, 109712 (2020).
- N. Neophytou, V. Vargiamidis, S. Foster, P. Graziosi, L. Oliveira, D. Chakraborty, Z. Li, M. Thesberg, H. Kosina, N. Bennett, and G. Pennelli, *Eur. Phys. J. B* **93**, 213 (2020).
- S. Wolf, N. Neophytou, and H. Kosina, *J. Appl. Phys.* **115**(20), 204306 (2014).
- S. Wolf, N. Neophytou, Z. Stanojevic, and H. Kosina, *J. Electron. Mater.* **43**(10), 3870–3875 (2014).
- D. Chakraborty, L. de Sousa Oliveira, and N. Neophytou, *J. Electron. Mater.* **48**(4), 1909–1916 (2019).
- A. Mittal and S. Mazumdar, *J. Heat Transfer* **132**, 052402 (2010).
- Y. C. Hua and B. Y. Cao, *J. Comput. Phys.* **342**, 253–266 (2017).
- K. Kadoya, N. Matsunaga, and A. Nagashima, *J. Phys. Chem. Ref. Data* **14**, 947–970 (1985).